PNAS RESEARCH ARTICLE | BIOPHYSICS AND COMPUTATIONAL BIOLOGY OPEN ACCESS

Bipartite binding of the intrinsically disordered scaffold protein JIP1 to the kinase JNK1

Thibault Orand[a], Elise Delaforge[a], Alexandra Lee[b], Jaka Kragelj[a,1], Maud Tengo[a], Laura Tengo[a,2], Martin Blackledge[a], Elisabetta Boeri Erba[a], Roger J. Davis[b], Andrés Palencia[c,3], and Malene Ringkjøbing Jensen[a,3]

Affiliations are included on p. 11.

Edited by Adriaan Bax, NIH, Bethesda, MD; received October 1, 2024; accepted January 18, 2025

Scaffold proteins are key players in many signaling pathways where they ensure spatial and temporal control of molecular interactions by simultaneous tethering of multiple signaling components. The protein JIP1 acts as a scaffold within the c-Jun N-terminal kinase (JNK) signaling pathway by assembling three kinases, MLK3, MKK7, and JNK, into a macromolecular complex that enables their specific activation. The recruitment of these kinases depends on the 450-amino acid intrinsically disordered tail of JIP1, however, the structural details of this tail and the molecular mechanisms by which it binds kinases have remained elusive. Here, we provide an atomic resolution structural description of the JIP1 tail, and we study its interaction with the kinase JNK1. Using NMR spectroscopy, we show that JNK1 not only engages with the well-known docking site motif (D-motif) of JIP1, but also interacts with a noncanonical F-motif. We determine the crystal structure of the JIP1–JNK1 complex at 2.35 Å resolution revealing a bipartite binding mode of JIP1. Our work provides insights into the sequence determinants of F-motifs suggesting that these motifs may be more prevalent in JNK substrates than previously recognized. More broadly, our study highlights the power of NMR spectroscopy in uncovering kinase interaction motifs within disordered scaffold proteins, and it paves the way for atomic-resolution interaction studies of JIP1 with its multitude of interaction partners.

mitogen-activated protein kinases | JIP1 | JNK | motif tethering | local effective concentration

Significance

The scaffold protein JIP1 plays a key role in the c-Jun N-terminal kinase (JNK) signaling pathway by facilitating the colocalization of multiple kinases, thereby ensuring their precise and efficient activation. To gain insights into the molecular mechanisms of JIP1 function, we obtained an atomic-resolution structural description of its 450-amino acid intrinsically disordered tail and studied its interaction with the kinase JNK1. We find that JIP1 exploits a bipartite binding mechanism, involving the well-established D-motif and a noncanonical F-motif. This study highlights the importance of atomic-resolution approaches in uncovering kinase binding motifs in long intrinsically disordered substrates, which cannot be predicted by sequence analysis alone.

Mammalian cells are estimated to contain hundreds of millions of individual protein molecules with as many as 10% of these involved in signal transduction (1, 2). It is therefore remarkable that cells can correctly, and with very high fidelity, process all the signaling information they constantly receive. Over the past three decades, it has become increasingly clear that cells can achieve spatial and temporal control of molecular interactions through the use of scaffold proteins (3–6). Scaffold proteins assemble relevant components of a given pathway, for example kinases, into higher-order complexes thereby ensuring signaling specificity through enforced proximity or tethering (7, 8). Scaffold proteins are in general extremely diverse, yet they are architecturally related as they are often composed of multiple folded domains interspersed with intrinsically disordered regions (IDRs) (9). Interestingly, some scaffold proteins display an unusual amount of intrinsic disorder (>60% of the total sequence), posing significant challenges for structural biology due to their highly dynamic nature (10). This is the case for the JNK-interacting protein 1 (JIP1) that acts as a scaffold protein in the stress-activated c-Jun N-terminal kinase (JNK) pathway (11, 12). Within this pathway, JIP1 recruits the three kinases JNK, MKK7, and the mixed-lineage kinase 3 (MLK3), thereby mediating specific and sequential activation of the bound kinases (13–15). The recruitment of these kinases depends on the 450-amino acid N-terminal IDR of JIP1, and complex formation has been shown to be regulated by the phosphorylation state of this disordered tail (16–18).

Currently, the only available structural information on the IDR of JIP1 is a crystal structure of the docking site motif (D-motif) of JIP1 in complex with JNK1 (19) or JNK3 (20). D-motifs are found within the interactome of mitogen-activated protein kinases (MAPKs), where they mediate the recruitment of specific MAPKs (JNK, ERK, and p38) to upstream kinases, phosphatases, substrates, and scaffold proteins (21, 22). D-motifs are composed of three hydrophobic residues and of up to five basic residues according to the consensus sequence: $K/R_{1\text{-}5}$–$X_{0\text{-}5}$–Φ_L–$X_{1\text{-}3}$–Φ_A–X–Φ_B, where X is any amino acid type and Φ is a hydrophobic residue (23–28). This sequence binds to the D-motif recruitment site (DRS), a conserved region on the surface of the C-lobe of the MAPKs (29, 30). The hydrophobic submotif (composed of Φ_L, Φ_A, and Φ_B) binds to a groove composed of three hydrophobic pockets within the DRS, while the basic residues interact with the

Author contributions: T.O., E.D., R.J.D., and M.R.J. designed research; T.O., E.D., A.L., J.K., M.T., L.T., E.B.E., and M.R.J. performed research; T.O., E.D., A.L., M.B., E.B.E., R.J.D., A.P., and M.R.J. analyzed data; and T.O., E.D., and M.R.J. wrote the paper.

The authors declare no competing interest.

This article is a PNAS Direct Submission.

[1]Present address: Slovenian NMR Centre, National Institute of Chemistry, Ljubljana SI-1000, Slovenia.

[2]Present address: European Molecular Biology Laboratory, Grenoble 38042, France.

[3]To whom correspondence may be addressed. Email: andres.palencia@inserm.fr or malene.jensen@ibs.fr.

This article contains supporting information online at https://www.pnas.org/lookup/suppl/doi:10.1073/pnas.2419915122/-/DCSupplemental.

Published February 25, 2025.

negatively charged common docking (CD) groove. The nature and spacing of amino acids within the D-motif are believed to determine specificity toward JNK, ERK, or p38 (25, 31).

In addition to D-motifs, F-motifs have also been shown to play a role in the recognition of MAPKs through binding to the F-motif recruitment site (FRS) located below the catalytic site (32). F-motifs were initially discovered in the ETS (E26 Transformation Specific) family of transcription factors leading to the definition of an F-motif consensus sequence: FXFP (where X is any amino acid) (33–36). The presence of F-motifs in MAPK-interacting proteins may, alongside D-motifs, provide additional interaction specificity and functional roles, such as regulation of substrate phosphorylation (37–40). However, more experimental studies are needed to identify these motifs and to confirm their direct involvement in MAPK binding and signaling regulation.

Here, we unveil how the intrinsically disordered tail of the JIP1 scaffold protein interacts with JNK1. Using NMR spectroscopy, we present an atomic-resolution structural description of the 450-amino acid IDR of JIP1. In addition to the well-characterized D-motif, we identify a noncanonical F-motif located 55 residues C-terminally of the D-motif. Although the F-motif shows weak binding affinity for JNK1, tethering of JIP1 to JNK1 via the high-affinity D-motif significantly enhances the local effective concentration of the F-motif near the FRS, resulting in predominantly bipartite binding of JIP1 to JNK1. To reveal the structural basis for this interaction, we solve the crystal structure of the JIP1–JNK1 complex at 2.35 Å resolution. Our work highlights how MAPKs can exploit multiple motifs, even separated by long disordered linkers, for binding to their interaction partners. More generally, our work provides insights into the molecular recognition mechanisms exploited by IDRs and, at the same time, paves the way for atomic resolution studies of the interaction of the JIP1 scaffold protein with its various partners.

Results

Atomic Resolution Description of the 450-Amino Acid Intrinsically Disordered Tail of JIP1. The scaffold protein JIP1 contains an N-terminal cysteine-rich IDR, an SH3 domain with a noncanonical function (dimerization) (41, 42), and a phosphotyrosine interaction domain (PID, Fig. 1*A*). This domain organization is supported by a disorder prediction by IUPRED (43) showing a high disorder score for the N-terminal 450 amino acids of JIP1 (Fig. 1*B*). To obtain structural insight into the IDR of JIP1, we studied this domain using NMR spectroscopy. We obtained the backbone spectral assignment by a divide-and-conquer strategy (44, 45) (*SI Appendix*, Fig. S1). Thus, the assignments of shorter, overlapping constructs ($JIP1_{1–145}$, $JIP1_{116–266}$, $JIP1_{245–372}$, and $JIP1_{353–553}$, with the subscripts indicating construct residue boundaries) were obtained and transferred to longer constructs ($JIP1_{1–266}$, $JIP1_{1–372}$, and $JIP1_{1–450}$) by comparison of their $^{1}H–^{15}N$ HSQC spectra (Fig. 1 *C–E* and *SI Appendix*, Fig. S2 *A–C*). This approach was successful and allowed assignment of the ^{1}H-^{15}N HSQC spectra of $JIP1_{1–266}$, $JIP1_{1–372}$, and $JIP1_{1–450}$, however, we observed small, nonnegligible chemical shift perturbations (CSPs) when comparing the NMR spectra of $JIP1_{1–145}$ and $JIP1_{116–266}$ with the corresponding longer construct, $JIP1_{1–266}$ (Fig. 1*C*). These CSPs were not observed when comparing $JIP1_{1–266}$ with $JIP1_{1–372}$ nor $JIP1_{1–372}$ with $JIP1_{1–450}$ (Fig. 1 *D* and *E* and *SI Appendix*, Fig. S2 *D–F*). Residues 1 to 120 of JIP1 have a net negative charge of –19 (27 negatively charged residues), while residues 121 to 200 have a high content of positively charged residues with a net positive charge of +7 (Fig. 1*F* and *SI Appendix*, Fig. S2*G*). The residues showing the largest CSPs belong to these charged regions of the JIP1 sequence suggesting the presence of long-range interactions between the negatively charged N terminus and the positively charged region around residues 121 to 200 (Fig. 1 *G* and *H*).

The SSP (47), derived from the experimental Cα and Cβ chemical shifts (*SI Appendix*, Fig. S3), reveal that the IDR of JIP1 is globally disordered with SSP scores below 0.5 along the entire sequence (Fig. 1*I*). We, however, note the presence of several regions with α-helical (residues 50 to 70, 80 to 90 and 110 to 120 and 170 to 180) and β-strand (residues 10 to 20, 120 to 140, and 245 to 300) propensities. The data therefore show that the JIP1 IDR is predominantly disordered with interspersed secondary structure elements of modest propensity.

The Disordered Tail of JIP1 Harbors Two JNK1-Binding Motifs. The interaction between JIP1 and JNK1 was initially studied by measuring ^{1}H-^{15}N HSQC spectra of $JIP1_{116-266}$ (the shortest construct comprising the D-motif) with increasing amounts of JNK1 (Fig. 2*A*). $JIP1_{116–266}$ shows extensive intensity loss of all resonances from residues 155 to 220 (Fig. 2 *A* and *B*), without displaying significant chemical shift perturbations (*SI Appendix*, Fig. S4*A*). Surprisingly, the observed intensity loss extends well beyond the D-motif (located at residues 157 to 167) suggesting the presence of additional JNK1-binding features on the JIP1 scaffold. To define more precisely the JNK1-interacting regions, we compared ^{15}N $R_{1\rho}$ relaxation rates (48) of $JIP1_{116–266}$ in the absence and presence of 25% (molar ratio) of JNK1 (Fig. 2*C*). The $R_{1\rho}$ relaxation rates only increase slightly for residues within the D-motif and more significantly at a second site (residues 205 to 220) located C-terminal to the D-motif. These two sites also show modest conformational exchange contributions to the transverse relaxation as measured by Carr-Purcell-Meiboom-Gill (CPMG) relaxation dispersion experiments (Fig. 2*D*) (49). The extensive intensity loss observed within the D-motif, the modest exchange contributions to the transverse relaxation rate, and the small increase in the $R_{1\rho}$ relaxation rates suggest that residues within the D-motif are in, or close to, the slow-exchange regime on the NMR chemical shift time scale. The second site shows larger increases in $R_{1\rho}$ relaxation and more significant exchange contributions upon addition of JNK1 placing residues in this motif in the slow-to-intermediate exchange regime. Collectively, our data demonstrate that JNK1 binds to two separate motifs on the $JIP1_{116–266}$ sequence with the intervening linker being dynamically restricted as evidenced by the simultaneous drop in signal intensities throughout the region encompassing residues 155 to 220.

JIP1 Contains a Noncanonical F-motif. The sequence corresponding to the second binding site, ^{211}ICLSDEL^{217}, contains three spaced hydrophobic residues, and we, therefore, investigated whether the interaction at this site is hydrophobically driven. A simultaneous mutation of both I211 and L213 to alanine (hereafter named the IL mutant), completely abolished binding of JNK1 as evidenced from the absence of line broadening within the second motif upon addition of JNK1 (Fig. 2*E*). These results clearly show that binding of JNK1 at the second site is hydrophobically driven and identify either I211 and/or L213 as crucial residues for the interaction. Next, we abolished binding to the canonical D-motif through the introduction of four single point mutations (R160E, P161A, L164A, L166A, hereafter named the RPLL mutant) (50). JNK1-binding to the D-motif was efficiently abrogated as shown by the absence of intensity loss within the D-motif upon addition of JNK1 (Fig. 2*F*). Binding was, however, still observed to the second

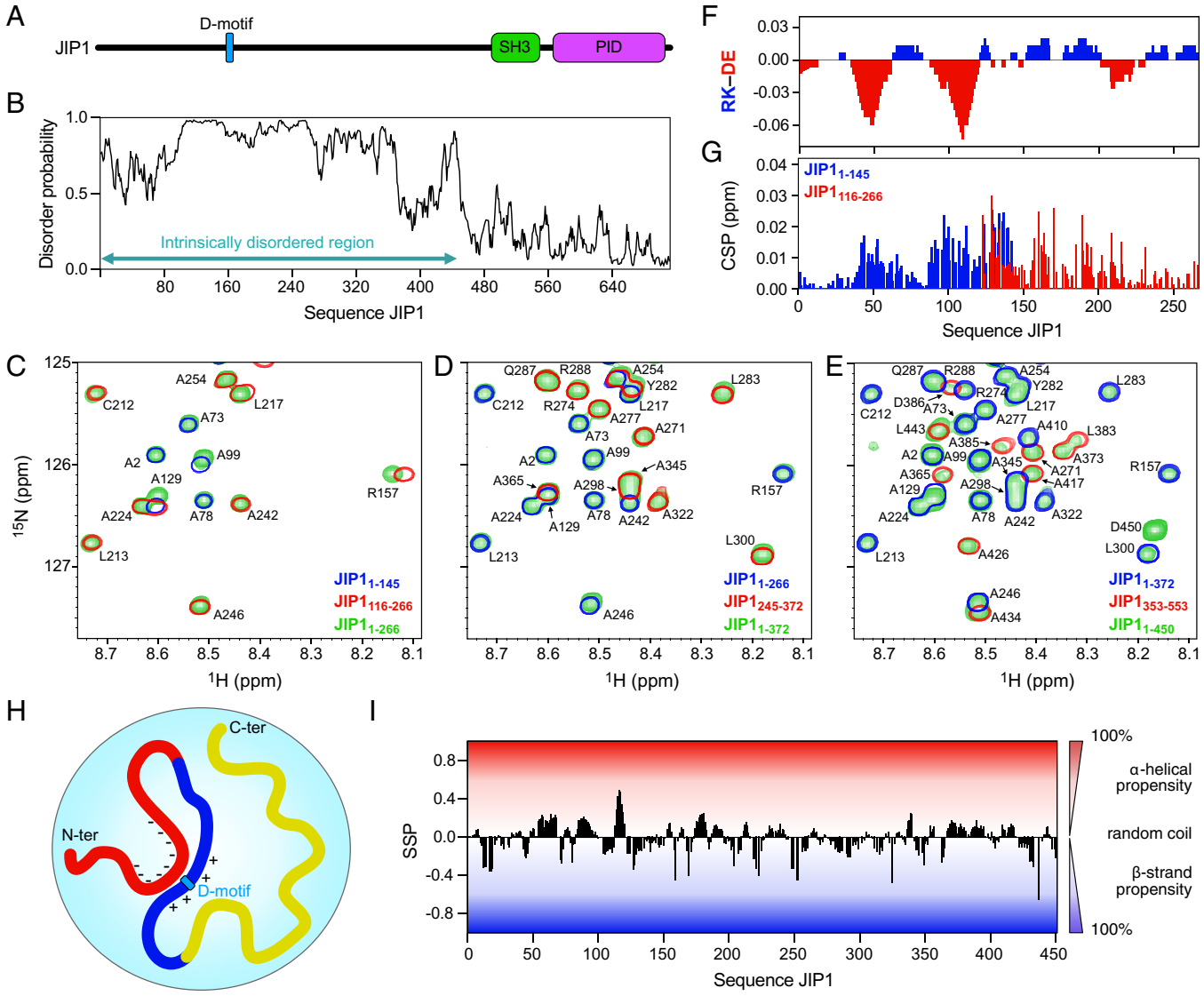

Fig. 1. Secondary structure propensities (SSP) and long-range interactions in the intrinsically disordered tail of JIP1. (*A*) Schematic representation of the domain organization of JIP1. (*B*) Disorder prediction of JIP1 with the intrinsically disordered tail covering 450 amino acids. (*C*) Superposition of a region of the ^{1}H-^{15}N HSQC spectra of JIP1$_{1–145}$ (blue), JIP1$_{116–266}$ (red), and JIP1$_{1–266}$ (green). Labels indicate the assignments of the different peaks. Small CSPs are observed between the shorter constructs (1 to 145 and 116 to 266) and the longer construct (1 to 266). (*D*) Superposition of a region of the ^{1}H-^{15}N HSQC spectra of JIP1$_{1–266}$ (blue), JIP1$_{245–372}$ (red), and JIP1$_{1–372}$ (green). (*E*) Superposition of a region of the ^{1}H-^{15}N HSQC spectra of JIP1$_{1–372}$ (blue), JIP1$_{353–553}$ (red), and JIP1$_{1–450}$ (green). (*F*) Charge distribution in JIP1$_{1–266}$ smoothed over 15 residues with arginines and lysines counting as +1 and aspartic acids and glutamic acids counting as −1 calculated using IDDomainSpotter (46). (*G*) Combined ^{15}N and ^{1}H CSPs when comparing the ^{1}H-^{15}N HSQC spectra of JIP1$_{1–145}$ with JIP1$_{1–266}$ (blue) and of JIP1$_{116–266}$ with JIP1$_{1–266}$ (red). Data for the six C-terminal residues in JIP1$_{1–145}$ and for the seven N-terminal residues in JIP1$_{116–266}$ were omitted from the plot to minimize construct boundary effects on the CSPs. (*H*) Schematic representation of the long-range interactions within the IDR of JIP1, as determined from CSPs between different JIP1 constructs. The negatively charged N terminus makes electrostatic contacts with the positively charged region around the D-motif. (*I*) SSP of JIP1$_{1–450}$ calculated from the experimental ^{13}Cα and ^{13}Cβ chemical shifts.

site showing that it can interact with JNK1 independently of the D-motif (Fig. 2*F* and *SI Appendix*, Fig. S4*B*).

Finally, we investigated whether the second site corresponds to an F-motif thereby recognizing the conserved hydrophobic groove of the FRS of JNK1. We carried out a competition experiment using the catalytic domain of the MKP7 phosphatase, which binds to the FRS of JNK1 via a ^{285}FNFL^{288} motif located in its C-terminal helix (51). First, we determined the dissociation constant, K_d, of the MKP7–JNK1 complex by isothermal titration calorimetry (ITC), obtaining a value of 1.1 μM, and we carried out a control experiment showing no interaction of MKP7 with JIP1$_{116–266}$ (*SI Appendix*, Fig. S5 and Table S1). Next, we compared intensity profiles of JIP1$_{116–266}$ with 70% JNK1 without and with 70% MKP7 (Fig. 2*G*). Off-competition of JIP1$_{116–266}$ from JNK1 is observed at the second site showing that this motif binds to the FRS, while leaving the interaction with the D-motif nearly unperturbed. We note that the intensities do not fully recover for residues within the second site upon addition of MKP7. This residual line broadening may arise from incomplete off-competition or from the continued anchoring of JNK1 to the D-motif, as supported by our experiments showing more complete off-competition of the second motif by MKP7 in the context of the RPLL mutant (Fig. 2*H*). Collectively, our results demonstrate that the second site should be characterized as a noncanonical F-motif, given the absence of phenylalanine residues within the motif sequence.

The F-motif of JIP1 Folds into a Helical Structure upon Binding to JNK1. To evaluate the contribution from the extended binding region to the affinity of the interaction between JNK1 and JIP1, we

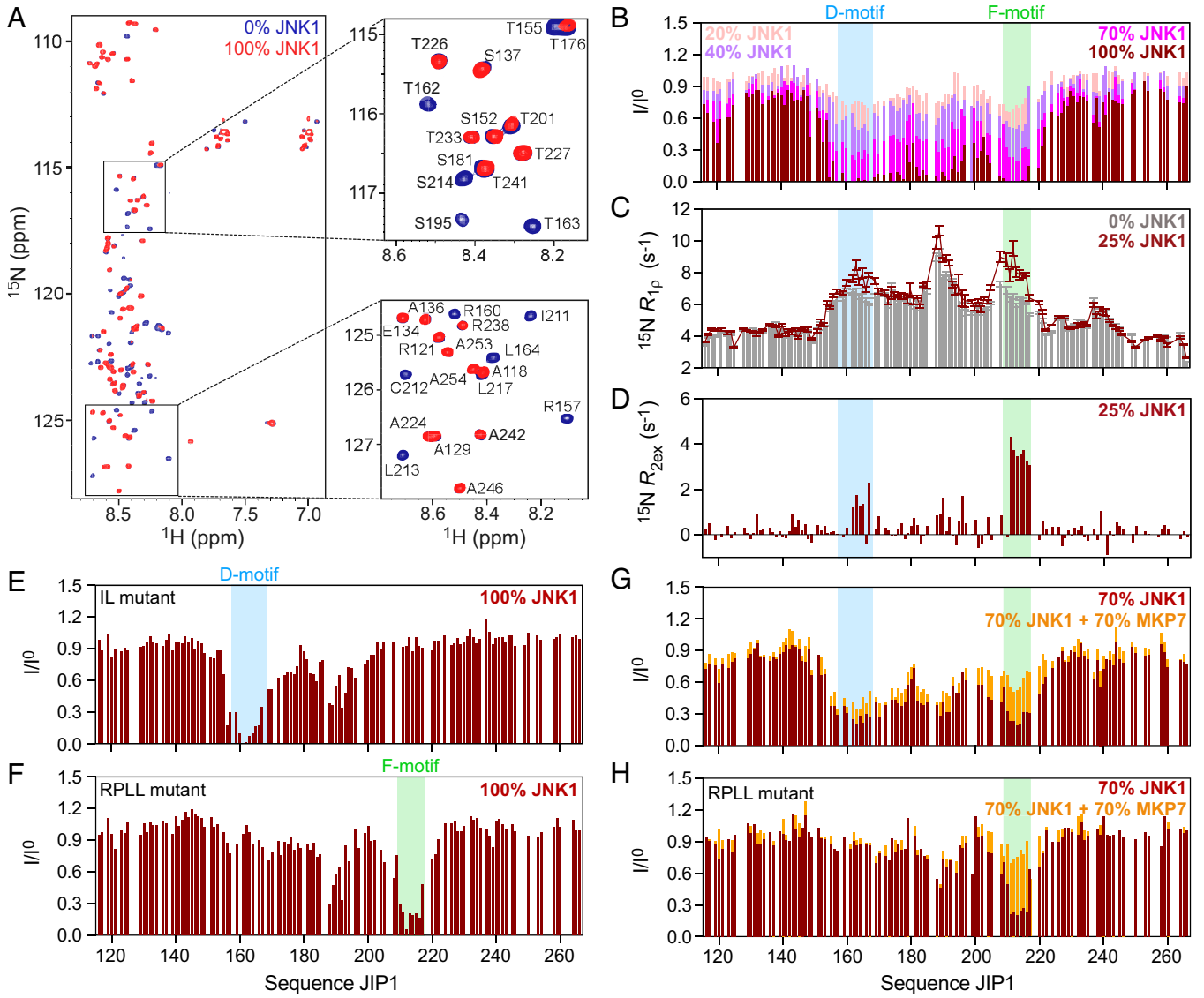

Fig. 2. Interaction between JIP1$_{116–266}$ and JNK1 reveals a new kinase binding site. (*A*) Superposition of the ^{1}H-^{15}N HSQC spectra of JIP1$_{116–266}$ (blue) and of JIP1$_{116–266}$ with 100% (molar ratio) of JNK1 (red). Two zooms are shown with labels corresponding to the assignment of the different peaks. (*B*) Intensity profile (I/I^0) of JIP1$_{116–266}$ (50 μM) obtained from the NMR signal intensities in the ^{1}H-^{15}N HSQC spectrum of the free state of JIP1$_{116–266}$ (I^0) and of JIP1$_{116–266}$ with different molar ratios of JNK1 (I): 20% (light pink), 40% (purple), 70% (magenta), and 100% (red). (*C*) ^{15}N $R_{1\rho}$ relaxation rates measured at a ^{1}H frequency of 600 MHz and 5 °C of JIP1$_{116–266}$ (180 μM, gray bars) and of JIP1$_{116–266}$ with 25% JNK1 (red). (*D*) ^{15}N conformational exchange contributions, R_{2ex}, extracted from CPMG relaxation dispersion data acquired at 700 MHz and 5 °C of JIP1$_{116–266}$ (200 μM) with 25% JNK1. (*E*) Intensity profile of the IL mutant of JIP1$_{116–266}$ (50 μM) in the presence of 100% JNK1. (*F*) Intensity profile of the RPLL mutant of JIP1$_{116–266}$ (50 μM) in the presence of 100% JNK1. (*G*) Intensity profile of JIP1$_{116–266}$ (100 μM) in the presence of 70% JNK1 (red) and of 70% JNK1 + 70% MKP7 (orange). (*H*) Intensity profile of the RPLL mutant of JIP1$_{116–266}$ (100 μM) in the presence of 70% JNK1 (red) and with 70% JNK1 + 70% MKP7 (orange). All percentages are molar ratios with respect to the JIP1 concentration.

compared ITC titrations of JNK1 with JIP1$_{116–266}$ and with a peptide corresponding to the D-motif of JIP1 (^{157}RPKRPTTLNLF^{167}). The ITC experiments show that the D-motif peptide binds with a K_d of 217 nM to JNK1 (Fig. 3*A*), while JIP1$_{116–266}$ shows a 2.7-fold higher affinity (K_d = 81 nM, Fig. 3*B*). This increase in binding affinity is accompanied by a substantial increase in the binding enthalpy ($\Delta\Delta H$ = 4.0 kcal/mol, *SI Appendix*, Table S1) suggesting that additional contacts with JNK1 occur in the sequence beyond the D-motif, in agreement with our NMR data.

To directly probe the binding contribution from the F-motif, we performed ITC experiments on the IL mutant of JIP1$_{116–266}$ (Fig. 3*C*). JIP1$_{116–266}$ and its IL mutant show very similar dissociation constants (K_d = 81 nM vs. 82 nM) and binding enthalpies (ΔH = −11.6 kcal/mol vs. −10.7 kcal/mol, *SI Appendix*, Table S1). The data therefore do not reveal an apparent contribution from the F-motif to the total binding affinity of the JIP1–JNK1 complex. We then carried out ITC titrations using the RPLL mutant of JIP1$_{116–266}$ (Fig. 3*D*). These experiments reveal no apparent interaction of JNK1 with JIP1 showing that the F-motif alone has a weak intrinsic binding affinity. To confirm these results, we carried out native mass spectrometry (MS) experiments. Accordingly, MS assesses a 1:1 stoichiometry when using JIP1$_{116–266}$ and its IL mutant, while the RPLL mutant of JIP1$_{116-266}$ shows no apparent complex formation (*SI Appendix*, Fig. S6 *A–C*).

To gain insight into the structure of the F-motif adopted upon binding to the FRS, we measured ^{15}N $R_{1\rho}$ and CPMG relaxation dispersion experiments on the RPLL mutant of JIP1$_{116–266}$ in the presence of 15% (molar ratio) of JNK1 (Fig. 3 *E* and *F*). This mutant allows to probe the binding contribution from the F-motif alone without the influence of the D-motif. We analyzed the relaxation dispersion data simultaneously for multiple residues within the F-motif according to a two-site exchange model (Fig. 3 *G–J*). The analysis yields a bound-state population of p_B = 1.6 ± 0.1% and an exchange rate constant of k_{ex} = 1,100 ± 100 s^{-1}

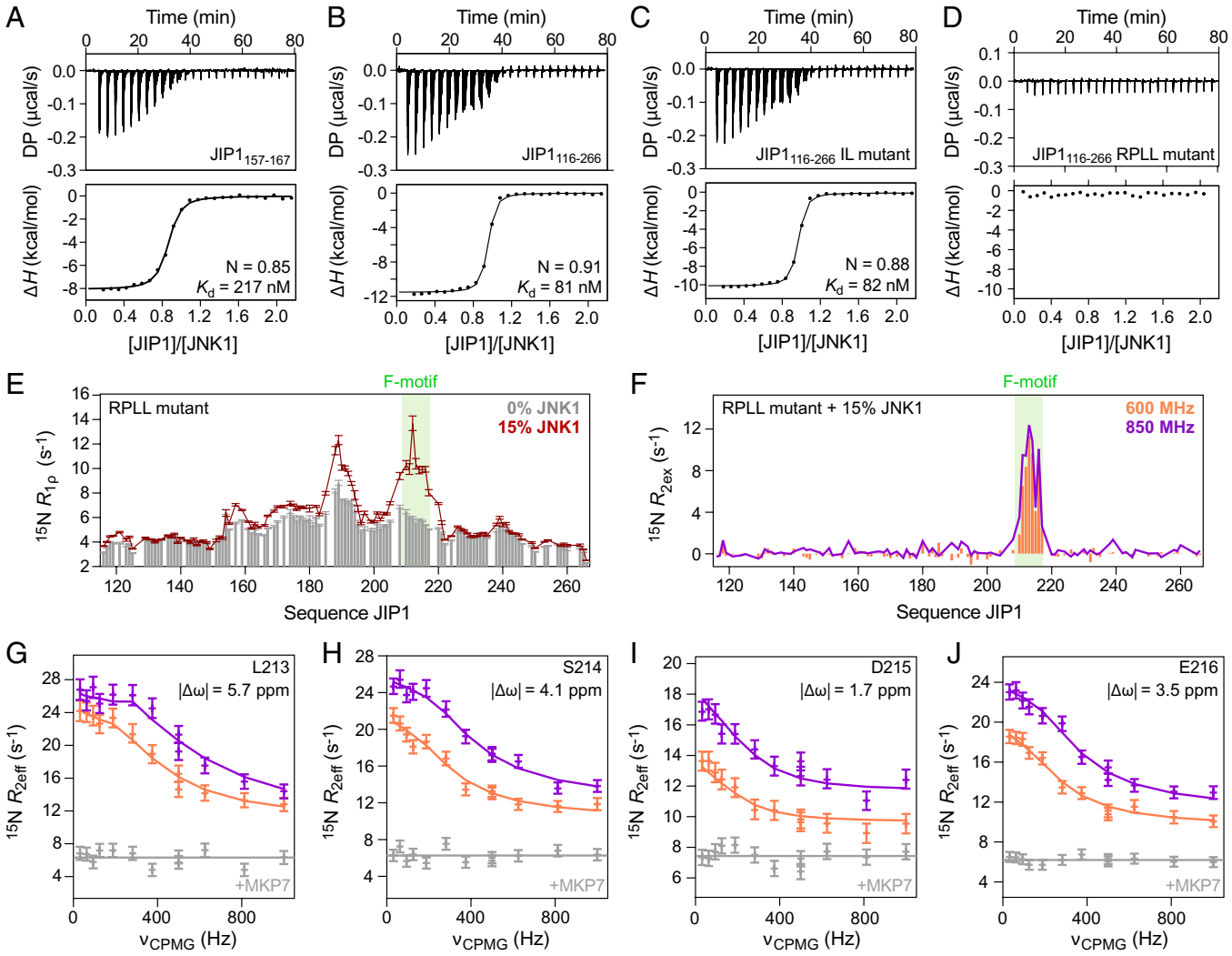

Fig. 3. Determination of the binding affinity of JIP1 for JNK1. (*A*) ITC data for binding of JNK1 to the D-motif peptide (residues 157 to 167) of JIP1. (*B*) ITC data for binding of JNK1 to $JIP1_{116-266}$. (*C*) ITC data for binding of JNK1 to the IL mutant of $JIP1_{116-266}$. (*D*) ITC data for binding of JNK1 to the RPLL mutant of $JIP1_{116-266}$. In *A–D*, representative ITC data are shown with raw injection heats (DP–differential power, *Upper*) and the corresponding specific binding isotherms (*Lower*). All ITC measurements were carried out in duplicates at 15 °C with JNK1 in the sample cell, and the data were analyzed according to a model with *n* independent binding sites. (*E*) ^{15}N $R_{1\rho}$ relaxation rates measured at a ^{1}H frequency of 600 MHz and 5 °C of the RPLL mutant of $JIP1_{116-266}$ (gray bars) and with 15% JNK1 (red). (*F*) ^{15}N conformational exchange contributions, R_{2ex}, extracted from CPMG relaxation dispersion data acquired at 600 MHz (orange) and 850 MHz (purple) at 5 °C of the RPLL mutant of $JIP1_{116-266}$ with 15% JNK1. (*G–J*) Analysis of ^{15}N relaxation dispersion data of the RPLL mutant of $JIP1_{116-266}$ (250 µM) with 15% JNK1 (orange–600 MHz, purple–850 MHz). The data were analyzed simultaneously for all residues within the F-motif according to a two-site exchange model (full drawn lines). Examples are shown for different residues within the F-motif (*G*–L213, *H*–S214, *I*–D215, *J*–E216) and the determined chemical shift differences (Δω) between their free and JNK1-bound form are reported. For comparison, the relaxation dispersion curves (600 MHz) are shown of the RPLL mutant in the presence of 70% JNK1 and 70% MKP7 (gray).

corresponding to kinetic rate constants of k_{off} = 1,082 s^{-1} and k_{on} = 4.8 × 10^5 $M^{-1}s^{-1}$ and a complex dissociation constant of K_D = 2.2 mM, in agreement with the absence of a detectable ITC signal (Fig. 3*D*). A control CPMG relaxation dispersion experiment, carried out on $JIP1_{116-266}$ in the presence of 70% JNK1 and 70% MKP7, shows flat dispersion curves proving that the observed exchange contributions arise from binding of the F-motif to the FRS of JNK1 (Fig. 3 *G–J*, gray data). The binding of JNK1 results in large ^{15}N chemical shift changes, Δω, within the F-motif (ranging from 1.7 to 5.7 ppm) suggesting an interaction mechanism involving folding-upon-binding (28). The residues in the F-motif show predominantly negative Δω values (*SI Appendix*, Fig. S7) (52) consistent with α-helical folding.

D-motif Tethering and Linker Interactions Result in High FRS Occupancy. We next set out to assess whether the structural context offered by the high-affinity D-motif compensates for the weak intrinsic JNK1-binding affinity of the F-motif. Indeed, the D-motif tethers JIP1 to JNK1, thereby increasing the local effective concentration (C_{eff}) of the F-motif near the FRS (Fig. 4*A*). In the absence of allosteric coupling between the DRS and the FRS, as previously determined for other MAPKs (53, 54), the forward rate constant for the transition from the single-tethered state of JIP1 to the double-tethered state is given by $k_{on}C_{eff}$, while the backward rate constant is k_{off} (Fig. 4*A*) (55). Here, k_{on} and k_{off} represent the binding and dissociation rate constants of the F-motif when D-motif tethering is absent, as determined from the CPMG relaxation dispersion data for the RPLL mutant of $JIP1_{116-266}$ (Fig. 3 *G–J*). The use of the RPLL mutant of $JIP1_{116-266}$ to quantify the dissociation constant, K_d, of the F-motif in the untethered system offers the advantage of preserving the structural context, thereby effectively accounting for potential interactions between the JIP1 linker and JNK1, which may be reinforced in the tethered system.

To determine the population of JIP1 in the double-tethered state, we estimated the value of C_{eff}. Using a WLC model (56) and the C_{eff} calculator (57), we obtained a value of $C_{eff,\,WLC}$ of 2.8 mM

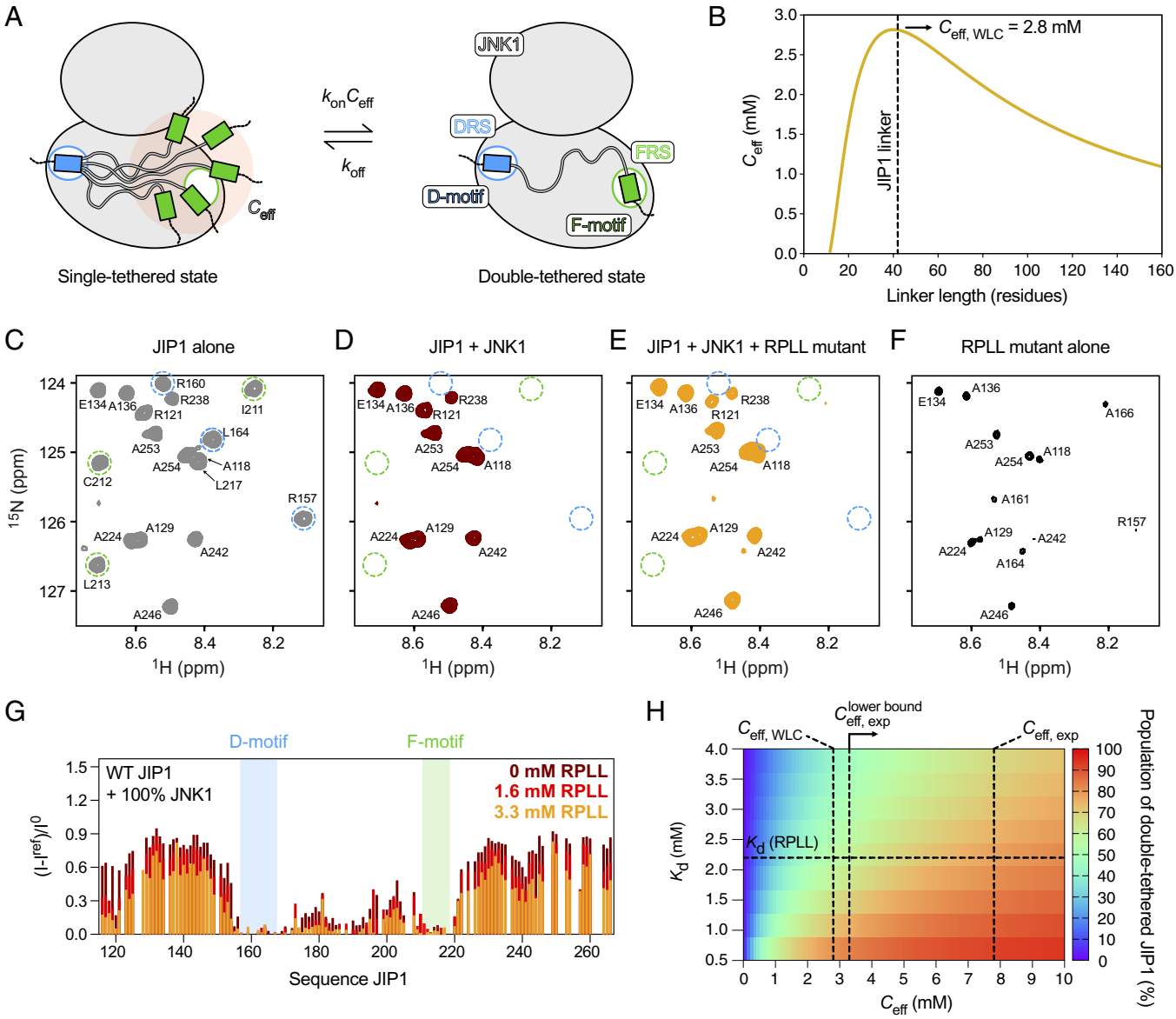

Fig. 4. D-motif tethering results in high occupancy of the FRS. (*A*) Schematic representation of the single- and double-tethered states of JIP1 upon interaction with JNK1. Within the single-tethered state, the F-motif experiences an increased local effective concentration, C_{eff}, in the vicinity of the FRS. The indicated rate constants, k_{on} and k_{off}, correspond to those measured for the F-motif in an untethered system (i.e., for the RPLL mutant of JIP1$_{116–266}$). (*B*) Calculation of C_{eff} using a worm-like chain (WLC) model as a function of linker length between the DRS and the FRS of JNK1. The length of the JIP1 linker is indicated by a dashed line. (*C*) Zoom on the ^{1}H-^{15}N HSQC spectrum of JIP1$_{116–266}$ (100 μM). Resonances corresponding to D- and F-motif residues are highlighted in blue and green dashed circles, respectively. (*D*) Zoom on the ^{1}H-^{15}N HSQC spectrum of JIP1$_{116–266}$ (100 μM) in the presence of JNK1 (100 μM). (*E*) Zoom on the ^{1}H-^{15}N HSQC spectrum of JIP1$_{116–266}$ (100 μM) in the presence of JNK1 (100 μM) and the RPLL mutant of JIP1$_{116–266}$ (3.3 mM). (*F*) Zoom on the ^{1}H-^{15}N HSQC spectrum (natural abundance) of the RPLL mutant of JIP1$_{116–266}$ (3.3 mM). (*G*) Intensity ratios, $(I - I^{ref})/I^{0}$, are presented for different concentrations of the RPLL mutant: 0 mM (dark red), 1.6 mM (red), and 3.3 mM (orange). Here, I is the intensity in the ^{1}H-^{15}N HSQC spectra of JIP1 with JNK1 and with different concentrations of the RPLL mutant, I^{0} is the intensity in the spectrum with only JIP1, and I^{ref} is the intensity in the spectra of the RPLL mutant alone (at natural abundance). For the dataset where the concentration of the RPLL mutant was 0 mM, I^{ref} was set to 0. The global decrease in intensity ratios for increasing concentrations of the RPLL mutant is attributed to viscosity effects. (*H*) Plot showing the population of double-tethered JIP1 as a function of the local effective concentration (C_{eff}) and the dissociation constant (K_d) of the untethered F-motif. A horizontal dashed line marks the K_d value measured for the RPLL mutant of JIP1$_{116–266}$. Vertical dashed lines represent C_{eff} calculated using the WLC model (2.8 mM), the lower-bound estimate of C_{eff} obtained from the competition experiments (3.3 mM) and C_{eff} estimated from CPMG relaxation dispersion data of JIP1$_{116–266}$ with 25% (molar ratio) of JNK1 (7.8 mM).

(Fig. 4*B*). The highest effective concentration predicted by this model corresponds to a linker length of 41 residues, closely matching the 43-residue linker in JIP1. To experimentally assess C_{eff}, we recorded ^{1}H-^{15}N HSQC spectra of ^{15}N JIP1$_{116–266}$ in the absence and presence of JNK1 (Fig. 4 *C* and *D*). We then attempted to displace the F-motif from JNK1 by introducing a large excess of the RPLL mutant of JIP1$_{116–266}$ (Fig. 4*E*). As these experiments required high concentrations of the competitor, we separately acquired natural abundance ^{1}H-^{15}N HSQC spectra of the RPLL mutant to account for its contribution to the observed NMR signal intensities (Fig. 4*F*) and to confirm that its conformational state remained similar to that observed at lower concentrations (*SI Appendix*, Fig. S8). The NMR signal intensities reveal minimal F-motif off-competition, even at competitor concentrations as high as 3.3 mM (Fig. 4*G*), allowing us to establish a lower bound for the experimentally determined C_{eff} at 3.3 mM.

To further quantify C_{eff}, we analyzed the CPMG relaxation dispersion data of wild-type JIP1$_{116–266}$ (200 μM) with 25% (molar ratio) of JNK1 according to a two-site exchange model (Fig. 2*D* and *SI Appendix*, Fig. S9). The analysis yields an excited

state population of p = 0.46 ± 0.04% and an exchange rate constant of k_{ex} = 1,300 ± 300 s^{-1}. The low population, the similarity of the exchange rate constant to that derived from the RPLL mutant of $JIP1_{116–266}$ (Fig. 3 *G–J*) and the excess of $JIP1_{116–266}$ in the sample, rule out a contribution from the exchange between the single- and double-tethered states of $JIP1_{116–266}$ to the observed relaxation dispersion. Instead, the relaxation dispersion arises from an exchange between free JIP1 and an FRS-bound state, where the DRS is occupied by a single-tethered JIP1 (*SI Appendix*, Fig. S9*E*). Using the dissociation constant of the untethered F-motif (RPLL mutant) and the population, p, of the excited state, we estimated the value of C_{eff} to be 7.8 mM (*SI Appendix*, Fig. S9).

The experimentally determined C_{eff} is significantly higher than the value predicted by the WLC model, suggesting that the linker between the D- and F-motif mediates contacts with JNK1. This hypothesis is supported by our ITC data, which show that the JNK1 binding affinity for $JIP1_{116–266}$ is approximately threefold higher than for a peptide containing only the D-motif (Fig. 3 *A* and *B*). The increase in affinity arises from linker interactions rather than F-motif binding, as demonstrated by the identical dissociation constants of $JIP1_{116–266}$ and its IL mutant (Fig. 3 *B* and *C*). Additional support for the presence of linker interactions comes from our NMR data. JNK1 binding causes a near-complete loss of NMR signal intensity in the linker between the D- and F-motif of $JIP1_{116–266}$ (Fig. 2*B*), an increase in the ^{15}N $R_{1\rho}$ relaxation rates in the linker of the RPLL mutant (Fig. 3*E*) as well as a decrease in intensities in the same region of the IL mutant (Fig. 2*E*). Although these linker interactions are likely nonspecific, they contribute positively to C_{eff} and play a role in stabilizing the double-tethered state of JIP1.

We calculated the population of the double-tethered state of JIP1 based on the determined local effective concentration (Fig. 4*H*). At a C_{eff} of 2.8 mM, as predicted by the WLC model, 56% of JIP1 is in the double-tethered state, while 44% remains single-tethered via the D-motif. Using the experimentally determined lower bound of 3.3 mM for C_{eff}, the double-tethered population is at least 60% and using the C_{eff} of 7.8 mM derived from the CPMG relaxation dispersion experiments, we obtain a population of double-tethered JIP1 of 78%. Collectively, our data demonstrate that tethering of JIP1 to JNK1 via the high-affinity D-motif, further reinforced by linker interactions, compensates for the weak intrinsic binding affinity of the F-motif, thereby making the double-tethered state of JIP1 predominant.

The F-motif of JIP1 Does Not Impact JNK1 Activation. To determine whether the F-motif is involved in JNK1 recruitment in cellulo, we transiently transfected mammalian COS-7 cells with JNK1 and JIP1 (wild-type or IL mutant). The two JIP1 variants show similar interactions with JNK1 by coimmunoprecipitation analysis (*SI Appendix*, Fig. S10*A*), in agreement with our ITC data (Fig. 3 *B* and *C*). When mutating the D-motif, the F-motif does not show a statistically significant interaction with JNK1 (*SI Appendix*, Fig. S10*A*). To determine whether the F-motif plays a role in JNK1 activation, we coexpressed JIP1 with components of the JNK pathway by transiently transfecting COS-7 cells with JIP1, JNK1 and with and without MLK3. Our data show that expression of MLK3, in the presence of JIP1, increases JNK1 activation (*SI Appendix*, Fig. S10*B*), in agreement with previous studies (12, 14, 58). The expression of JIP1 and JNK1 was monitored by immunoblot analysis and JNK1 activation was detected with an antibody specific to phosphorylation of the JNK1 activation loop. Similar JNK1 phosphorylation is observed for JIP1 and its IL mutant (*SI Appendix*, Fig. S10*B*) showing that the F-motif does not play a significant role in JNK1 activation.

Crystal Structure of the Bipartite JIP1–JNK1 Complex. To reveal the structural basis of the interaction of JNK1 with JIP1, we determined the crystal structure of JNK1 in complex with a peptide of JIP1 encompassing both the D- and F-motifs and the ATP analogue AMPPNP. To obtain diffracting crystals, the linker between the D- and F-motifs was shortened to reduce flexibility following an NMR-guided approach (*SI Appendix*, Fig. S11). The structure was solved at 2.35 Å resolution with the activation loop being fully visible in the electron density together with the D- and F-motif (Fig. 5*A* and *SI Appendix* Fig. S12*A* and Table S2). The activation loop is found in a "^{169}DFG^{171}-in" conformation which can be further subcategorized as a BLAminus conformation using the terminology of Modi and Dunbrack (59). While most kinases found in the BLAminus conformation display structural features consistent with an active kinase, our structure most likely captures JNK1 in an inactive conformation as the activation loop is unphosphorylated and does not adopt an extended conformation necessary for phospho-acceptor substrate binding (*SI Appendix*, Fig. S12*B*). The AMPPNP is found in the active site of the kinase where it makes multiple hydrogen bonds with JNK1 (*SI Appendix*, Fig. S12*C*). The D-motif adopts a conformation similar to previously solved crystal structures (19) with both electrostatic (Fig. 5 *A*, *Left*) and hydrophobic (Fig. 5 *B*, *Left*) binding features characteristic of canonical DRS/D-motif interactions (25).

The F-motif binds to the FRS and folds into a single helical turn upon binding to JNK1 consistent with the NMR relaxation dispersion data (Fig. 3 *G–J*). The structure of the F-motif is mainly stabilized by hydrophobic interactions mediated by the four residues I211, L213, L217, and P218 (Fig. 5 *B*, *Right*) and by four intermolecular hydrogen bonds: from the side chain of D215 to the side chain of T255 in JNK1, from the backbone of C212 to the side chain of Y230 in JNK1, from the backbone of S214 to the backbone of I197 in JNK1 and from the side chain of C212 to the backbone of T183 in JNK1 (Fig. 5 *A*, *Right*). None of the JIP1 hydrophobic residues reach the deep cavities of the FRS, as compared to the aromatic residues present in the F-motifs of the activating transcription factor 2 (ATF2, binding to double-phosphorylated p38α) and of MKP7 (binding to JNK1) (*SI Appendix*, Fig. S13), but they rather make side-contacts with the FRS pocket. Surprisingly, the polar residue S214 of JIP1 occupies the deep cavity of the FRS. A similar feature is observed for the complex between PEA-15 (15 kDa phosphoprotein enriched in astrocytes) and ERK2, where the polar side chain of R71 of PEA-15 occupies the deep FRS pocket of ERK2 (*SI Appendix*, Fig. S13 *J* and *K*). We evaluated the impact on JNK1 binding of three single point mutations (I211A, L213A, and L217A) in the F-motif of JIP1. Our results show that L213A and L217A impair the interaction, while I211A does not impact the binding to JNK1 (*SI Appendix*, Fig. S14). Nevertheless, full abrogation of the JNK1–JIP1 F-motif interaction is achieved with the double mutant I211A/L213A (Fig. 2*E*) suggesting that I211 also contributes to the interaction in the presence of L213.

To examine the evolutionary conservation of the F-motif, we performed a multiple sequence alignment of JIP1 sequences across vertebrates (*SI Appendix*, Fig. S15). The F-motif is highly conserved in Sarcopterygians (including notably mammals and birds), except in Lissamphibians, where L217 is replaced by a glycine. In contrast, we observe a significant loss of conservation of hydrophobic residues in Actinopterygians (ray-finned fishes), although this loss is less pronounced in Chondrichthyans (cartilaginous fishes).

The D- and F-motifs of JIP1 are well defined in the electron density (Fig. 5 *C* and *D*), however, the linker connecting the two motifs (16 residues in length in the construct used for X-ray crystallography) is not visible suggesting that it remains flexible and samples multiple conformations in complex with JNK1. It is likely that the native linker between the D- and F-motifs

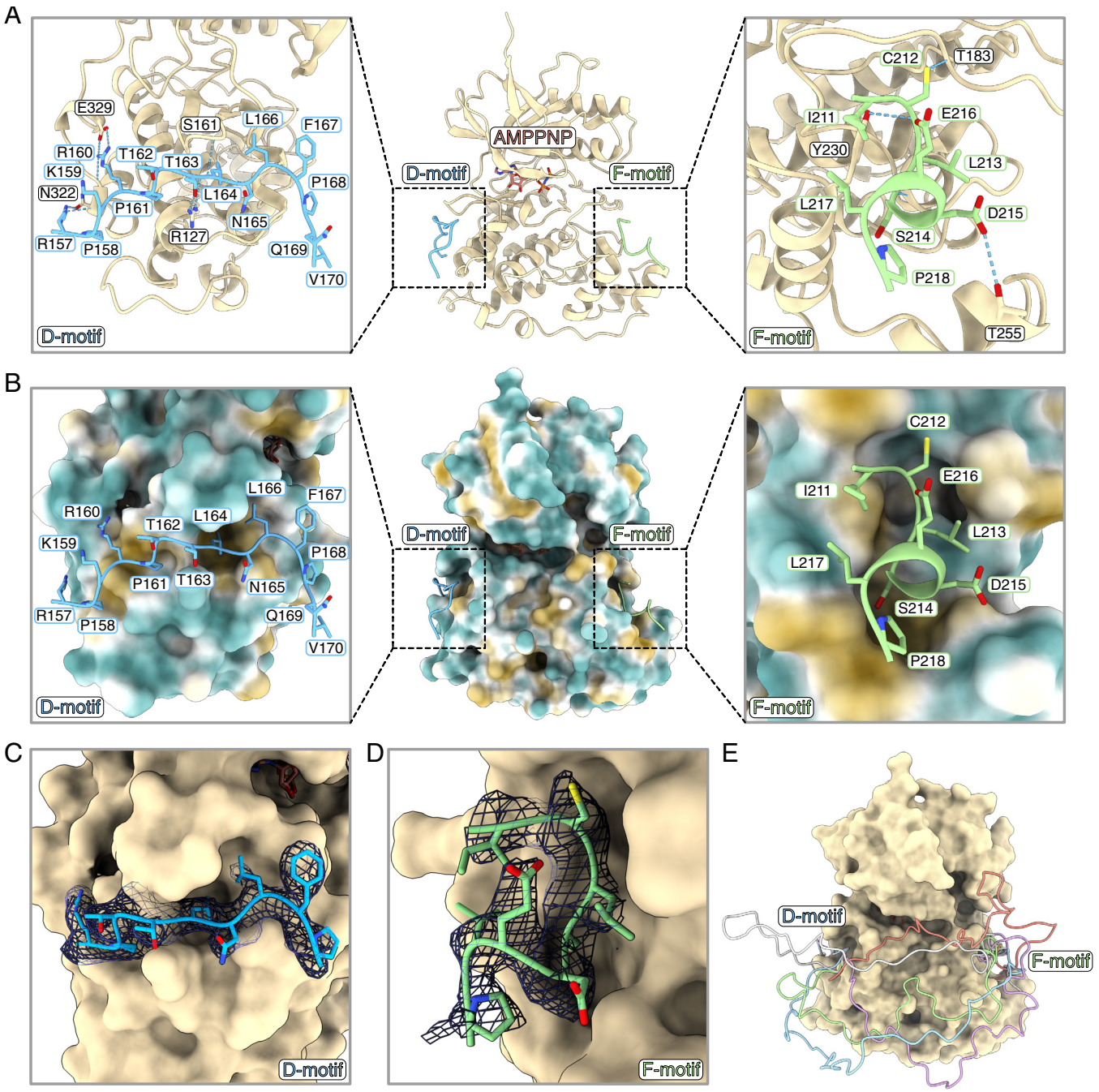

Fig. 5. Crystal structure of the JIP1–JNK1 complex. (*A*) Crystal structure of JNK1 (beige, ribbon model) in complex with JIP1 revealing the binding mode of both the D-motif (blue, zoom left) and the F-motif (green, zoom right). For the two zooms, intermolecular hydrogen bonds are indicated with blue dashed lines. The linker connecting the D- and F- motifs is not visible in the electron density. (*B*) The same as in panel *A*, but with JNK1 shown in surface representation and color-coded according to hydrophobicity (ranging from dark orange for the most hydrophobic potentials, through white, to teal for the most hydrophilic potentials). (*C*) Unbiased omit electron density map (Fo-Fc) of the D-motif contoured at 2σ. (*D*) Unbiased omit electron density map (Fo-Fc) of the F-motif contoured at 2σ. (*E*) Structural model of the JNK1–JIP1 complex where the native linker between the D- and F-motifs was constructed using a random coil sampling algorithm. The conformational ensemble illustrates the potential degree of disorder in the complex, disregarding contacts between the linker and JNK1.

(~43 residues in length) samples random coil conformations, as observed by the secondary structure propensities of JIP1 in isolation (Fig. 1*I*). Although our ITC and NMR data establish that the linker mediates stabilizing interactions with JNK1 in the complex, these contacts are likely nonspecific leading to a complex with a high degree of disorder, as illustrated in Fig. 5*E*.

The Disordered Tail of JIP1 Establishes Hydrophobic Contacts with JNK1. To obtain a more exhaustive view of the interaction of JNK1 with the full-length IDR of JIP1, we gradually increased the length of our JIP1 constructs and assessed the binding of JNK1 by NMR. Titrating increasing amounts of JNK1 into ^{15}N-labeled JIP1$_{1\text{-}266}$ reveals an additional binding region at the N terminus of JIP1 as evidenced by pervasive line broadening at residues 20 to 80 and significantly enhanced $R_{1\rho}$ relaxation rates of these residues compared to the free form of JIP1$_{1\text{–}266}$ (Fig. 6 *A* and *B*). We note that the N terminus of JIP1 can independently bind JNK1 (*SI Appendix*, Fig. S16 *A* and *B*), although the binding affinity is most likely in the millimolar range as the interaction is not readily detectable by ITC (*SI Appendix*, Fig. S16*C*). In agreement with this, MS of JIP1$_{1\text{-}145}$ shows a very low abundance 1:1 complex with JNK1 (*SI Appendix*, Fig. S6*D*),

while $JIP1_{1–266}$ displays mainly a 1:1 complex and a low abundance 1:2 (JIP1:JNK1) complex (*SI Appendix*, Fig. S6*E*). Despite the N-terminal interactions, $JIP1_{1–266}$ shows a 2.4-fold lower binding affinity for JNK1 compared to the shorter construct $JIP1_{116–266}$ (*SI Appendix*, Fig. S17*A*). This might be explained by a decrease in the accessibility of JNK1 to the D-motif due to the long-range interactions between the highly negatively charged N terminus of JIP1 and the positively charged D-motif (+3 net charge, Fig. 1*H*).

By extending the construct to $JIP1_{1–372}$, we identify an additional region (residues 265 to 350) that binds to JNK1. However, the $R_{1\rho}$ relaxation rates for this region show only a modest increase compared to the more pronounced changes observed at the N terminus of JIP1 (Fig. 6 *C* and *D*), suggesting a transient interaction with JNK1. In agreement with this, extending JIP1 up to residue 372 does not alter JNK1 binding affinity and thermodynamics compared to $JIP1_{1–266}$ (*SI Appendix*, Fig. S17*B*). Finally, we titrated JNK1 into the full-length IDR ($JIP1_{1–450}$). Line broadening effects are observed throughout the JIP1 IDR, and by comparison to the shorter JIP1 constructs, we observe additional JNK1-binding features in the region 370 to 430 (Fig. 6*E* and *SI Appendix*, Fig. S18*A*). Our NMR data acquired on constructs of different lengths therefore demonstrate that JNK1 binds with high affinity to the extended binding region via the D- and F-motifs of JIP1, while the N- and C-terminal tails of JIP1 transiently interact with the surface of JNK1. This

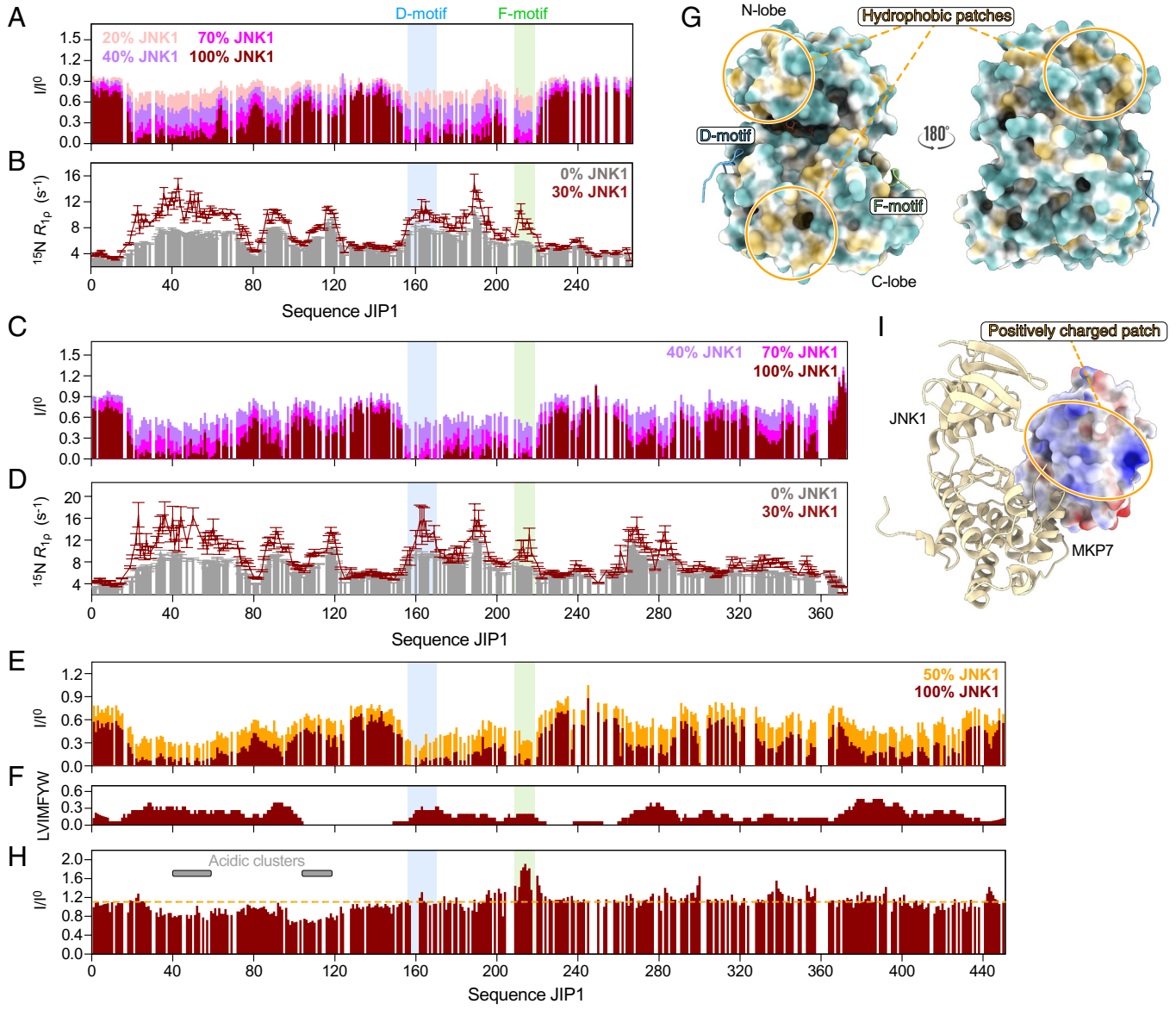

Fig. 6. JNK1 recruitment to JIP1 involves recognition of hydrophobic patches. (*A*) Intensity profile (I/I^0) of $JIP1_{1-266}$ (50 μM) obtained from the NMR signal intensities in the ^{1}H-^{15}N HSQC spectrum of the free state (I^0) and with different molar ratios of JNK1 (I): 20% (light pink), 40% (purple), 70% (magenta), and 100% (red). (*B*) ^{15}N $R_{1\rho}$ relaxation rates measured at a ^{1}H frequency of 600 MHz and 5 °C of $JIP1_{1-266}$ (gray bars) and with 30% JNK1 (red). (*C*) Intensity profile of $JIP1_{1-372}$ (70 μM) for different molar ratios of JNK1: 40% (purple), 70% (magenta), and 100% (red). (*D*) ^{15}N $R_{1\rho}$ relaxation rates measured at a ^{1}H frequency of 600 MHz and 5 °C of $JIP1_{1-372}$ (gray bars) and with 30% JNK1 (red). (*E*) Intensity profile of $JIP1_{1-450}$ (100 μM) with different molar ratios of JNK1: 50% (orange) and 100% (red). (*F*) Distribution of hydrophobic residues (Leu, Val, Ile, Met, Phe, Tyr, and Trp) along the sequence of $JIP1_{1-450}$. Each hydrophobic residue was counted as +1 and smoothed over 15 residues (red). (*G*) Structure of the JNK1–JIP1 complex with the surface of JNK1 color-coded according to hydrophobicity ranging from dark orange for the most hydrophobic potentials, through white, to teal for the most hydrophilic potentials. Predominant hydrophobic patches on the surface of JNK1 are highlighted in orange circles. (*H*) Competition experiment for binding to JNK1 between $JIP1_{1-450}$ and MKP7. The intensity profile (I/I^0) is shown where I corresponds to the intensities in a sample of $JIP1_{1-450}$ with 70% JNK1 and 70% MKP7, while I^0 corresponds to the intensities in a sample of $JIP1_{1-450}$ with 70% JNK1. Regions of JIP1 with I/I^0 values above the orange line are off-competed by MKP7, while regions with I/I^0 values below the orange line are reinforced in the presence of MKP7. The concentration of JIP1 was 80 μM. (*I*) Structure of the JNK1–MKP7 complex (PDB 4YR8) with JNK1 in cartoon representation and MKP7 in surface representation colored according to its electrostatic surface potential [scale: blue (positive) through white (neutral) to red (negative)].

binding profile is specific to JNK1, as demonstrated by the complete absence of interaction between JIP1 and bovine serum albumin that we used as a negative control (*SI Appendix*, Fig. S18*B*).

We analyzed the sequence composition around the regions of $JIP1_{1–450}$ that show significant intensity loss upon JNK1 binding. These regions share a common feature i.e., they contain local clusters of hydrophobic residues (Fig. 6*F*). The strong correlation between the location of these clusters and the observed line broadening upon interaction with JNK1 (Fig. 6 *E* and *F*) suggests that these clusters contact hydrophobic patches on the JNK1 surface. JNK1 displays a number of hydrophobic patches, including the DRS and the FRS, providing multiple possibilities for transient interactions with the hydrophobic clusters in JIP1 (Fig. 6*G*). We also carried out a competition experiment between $JIP1_{1-450}$ and MKP7 for binding to JNK1 (Fig. 6*H* and *SI Appendix*, Fig. S19). The data show that primarily the F-motif is displaced by MKP7, while other hydrophobic clusters in JIP1 rarely interact at the FRS. We note that upon interaction of $JIP1_{1–450}$ with JNK1 in the presence of MKP7, additional line broadening is observed at the level of the two acidic regions in the N terminus of JIP1 (Fig. 6*H*). These regions most likely interact with the positively charged patch on the surface of MKP7 within the ternary JIP1:JNK1:MKP7 complex (Fig. 6*I*), where JNK1 has its DRS occupied by JIP1 and its FRS occupied by MKP7.

In conclusion, our data support the following structural model for the JIP1–JNK1 complex. The recruitment of JNK1 to JIP1 occurs through the high-affinity D-motif and a "locking in" of the F-motif into the FRS. The positioning of the F-motif is guided by the linker between the D- and F-motifs ensuring a high local effective concentration of the F-motif near the FRS. The F-motif folds into a helical conformation occupying the hydrophobic groove at the FRS. Within this complex, the localized hydrophobic clusters in the N- and C-terminal regions of JIP1 interact with one or more hydrophobic patches on the surface of JNK1. Our results suggest that the hydrophobic clusters in the N-terminal region mediate more persistent and higher populated contacts with JNK1 than the C-terminal clusters that engage in more transient and dynamic interactions.

Discussion

In this work, we structurally characterize the complex between JNK1 and the 450-amino acid intrinsically disordered tail of the scaffold protein JIP1 using a combination of NMR, ITC, and X-ray crystallography. Importantly, we identify a previously unrecognized F-motif within JIP1 (^{211}ICLSDEL^{217}) that binds to the FRS of JNK1. Traditionally, F-motifs are defined as phenylalanine-rich sequences conforming to the consensus FXFP, where X represents any amino acid (33–36). However, studies employing positional scanning peptide arrays have refined our understanding of F-motif sequence preferences demonstrating that 1) ERK can accommodate aromatic residues other than phenylalanines at its FRS, 2) p38 can bind aliphatic amino acids at its FRS, with preferences varying among isoforms and 3) JNK generally displays surprisingly little sequence preferences at its FRS (60). Our work builds on these insights by revealing that aliphatic amino acids, specifically isoleucine and leucine, can bind to the FRS of JNK1 demonstrating that aromatic residues are not strictly required for FRS binding. The identification of this noncanonical F-motif in JIP1 paves the way for finding F-motifs in other JNK1 substrates through sequence searches and suggests that the presence of F-motifs in MAPK signaling may be more widespread than previously recognized.

The structural details of how known F-motifs bind to MAPKs remain poorly understood due to the limited availability of high-resolution structures. To date, only three crystal structures of MAPKs bound to partners at the FRS are available (*SI Appendix*, Fig. S13) (37, 51, 61). Two of these structures involve MAPKs complexed with the folded domains of their binding partners, MKP7 and PEA-15. In the catalytic domain of MKP7, the F-motif is embedded within its C-terminal helix (51), whereas PEA-15 lacks an F-motif and instead interacts with the FRS of ERK2 through two short helices connected by a loop (61). The third structure, representing a complex of ATF2 and double-phosphorylated p38α, features a linear F-motif (i.e. a motif embedded within an IDR of a substrate rather than in a folded binding partner) and is therefore comparable to our JIP1–JNK1 structure. Our crystal structure reveals that the F-motif in JIP1 adopts an α-helical conformation when bound to JNK1, resembling the ATF2-p38α structure (37). In the latter, ATF2 forms an α-helix allowing the two phenylalanines, Phe92 and Phe96, of the F-motif (^{92}FENEF^{96}) to occupy the hydrophobic pocket of the FRS of p38α. Although the limited structural data make broad generalizations difficult, these findings suggest that helical folding may be a common recognition mechanism for linear F-motifs binding to MAPKs.

The F-motif in JIP1 displays a weak intrinsic binding affinity for JNK1 (K_d of 2.2 mM). We show that tethering of JIP1 to JNK1 via the high-affinity D-motif compensates for this weak affinity, leading to a significant population (78%) of double-tethered JIP1 within the complex. The importance of motif tethering in multivalent interactions has been highlighted by several studies, which demonstrate remarkable increases in overall binding affinity driven by locally enhanced effective concentrations compared to the binding of individual motifs (55, 62, 63). A notable example is the disordered early region 1A (E1A), which binds to the retinoblastoma (Rb) protein via two binding motifs. Tethering of the two motifs results in a 4,000-fold increase in binding affinity compared to the binding of the individual motifs (55). Although tethering in our system does not result in an overall gain in binding affinity, its impact is evident as it confers a predominantly bipartite binding mode of JIP1 to JNK1.

All interaction experiments in this study were conducted using the inactive, unphosphorylated form of JNK1. Previous findings have demonstrated that the F-motif of ATF2 does not bind to inactive p38α and requires double-phosphorylation of the activation loop of p38α to reach a 25 μM binding affinity (37). Similarly, the F-motif of Elk-1 showed higher binding affinity toward active ERK2 than its inactive form (32). It is therefore possible that activation of JNK1 may induce conformational changes in the F-motif binding pocket, thereby modulating its affinity for the F-motif. To explore this hypothesis, future studies will be required using the phosphorylated, active form of JNK1.

The bipartite DRS/FRS binding mode has been observed previously for other MAPK complexes (37, 40, 61, 64, 65); however, this is an example for the JNK family. This particular binding mode has been proposed to have multiple functional roles such as providing additional specificity in the recognition of partner proteins for example by compensating for low-affinity DRS interactions. In the case of JIP1, the D-motif binds to JNK1 with nano-molar affinity, and it has been shown to be highly specific toward JNK1 compared to p38α and ERK2 (25). It is therefore unlikely that the F-motif in JIP1 plays the role of a "specificity regulator," in agreement with the similar JNK1 activation loop phosphorylation in COS-7 cells upon abolishing JNK1 binding to the F-motif. Instead, the F-motif could provide favorable spatial constraints for optimal phosphorylation of JIP1 by JNK1, as demonstrated previously for ERK2 phosphorylation of the Ets-1 and Elk-1 transcription factors (39, 66) and of the human Na^+/H^+ exchanger 1 (38). Indeed, JNK1 phosphorylates

eleven serines and threonines dispersed along the entire disordered tail of JIP1 and, importantly, some of these phosphorylation sites modulate JIP1 functions (16, 67, 68). Another potential function of the F-motif could be to control access to the FRS, by regulating for example dephosphorylation of JNK1 by the MKP7 kinase. Our competition experiments demonstrate that MKP7 readily displaces the F-motif of JIP1 from the FRS. However, this situation may differ in the active, double-phosphorylated form of JNK1, where the F-motif could acquire significantly higher affinity due to structural changes in the FRS pocket, as observed for the F-motif of ATF2 binding to p38α (37). Our study lays the foundation for future research to unravel the precise regulatory role of the identified noncanonical F-motif in JIP1.

Materials and Methods

Details of protein expression and purification procedures for all JIP1, JNK1, and MKP7 constructs; NMR spectral assignments, titrations, and relaxation experiments; samples and experimental setup for the ITC experiments to study the JIP1–JNK1 and JNK1–MKP7 interactions; crystallization conditions of the JIP1–JNK1 complex and processing of the X-ray diffraction data; calculations of local effective concentrations using the WLC model; and the plasmids, antibodies, and experimental protocols for the transfection assays and immunoblot analyses are provided in *SI Appendix*, *Materials and Methods*.

Data, Materials, and Software Availability. Protein structure data for the JNK1–JIP1 complex have been deposited in the Protein Data Bank database with the accession code 9FT9 (69). All ^{1}H, ^{13}C, and ^{15}N chemical shifts have been deposited in the BMRB database with accession numbers: JIP1$_{1\text{-}145}$ (BMRB: 52858) (70), JIP1$_{116\text{-}266}$ (BMRB: 52859) (71), JIP1$_{245\text{-}372}$ (BMRB: 52860) (72) and JIP1$_{353\text{-}553}$ (BMRB: 52861) (73). All other data are included in the manuscript and/or *SI Appendix*.

ACKNOWLEDGMENTS. We thank Pauline Juyoux for providing the JNK1 plasmid used for obtaining the crystal structure of the JNK1–JIP1 complex, Matthew Bowler for access to the MASSIF-1 beamline, Guillaume Hoffmann for help with initial X-ray data processing and Juan Cortés and Pau Bernadó for providing ensembles of the JIP–JNK1 complex. This work was funded by the Impulscience® programme of the Fondation Bettencourt Schueller (to M.R.J.), by the French Agence Nationale de la Recherche through ANR ScaffoldDisorder (to A.P. and M.R.J.) and by NIH grants DK107220 and DK112698 (to R.J.D.). T.O. was supported by a PhD fellowship from the doctoral school for chemistry and life sciences of the University Grenoble Alpes and from la ligue contre le cancer. J.K. was financed through a PhD fellowship from the IDPbyNMR Marie Curie action of the European Commission (Contract no 264257). This work used the platforms of the Grenoble Instruct-ERIC center (ISBG; UAR 3518 CNRS-CEA-UGA-EMBL) within the Grenoble Partnership for Structural Biology (PSB), supported by FRISBI (ANR-10-INBS-0005-02) and GRAL, financed within the University Grenoble Alpes graduate school (Ecoles Universitaires de Recherche) CBH-EUR-GS (ANR-17-EURE-0003). The Institut de Biologie Structurale acknowledges integration into the Interdisciplinary Research Institute of Grenoble.

Author affiliations: [a]Université Grenoble Alpes, Commissariat à l'Énergie Atomique et aux Énergies Alternatives, CNRS, Institut de Biologie Structurale, Grenoble 38044, France; [b]Program in Molecular Medicine, University of Massachusetts Medical School, Worcester, MA 01655; and [c]Institute for Advanced Biosciences, Structural Biology of Novel Targets in Human Diseases, INSERM U1209, CNRS UMR5309, Université Grenoble Alpes, Grenoble 38000, France

1. R. Milo, P. Jorgensen, U. Moran, G. Weber, M. Springer, BioNumbers—The database of key numbers in molecular and cell biology. *Nucleic Acids Res.* **38**, D750–D753 (2010).
2. R. Milo, What is the total number of protein molecules per cell volume? A call to rethink some published values. *Bioessays* **35**, 1050–1055 (2013).
3. K. Y. Choi, B. Satterberg, D. M. Lyons, E. A. Elion, Ste5 tethers multiple protein kinases in the MAP kinase cascade required for mating in S. cerevisiae. *Cell* **78**, 499–512 (1994).
4. J. A. Printen, G. F. Sprague, Protein-protein interactions in the yeast pheromone response pathway: Ste5p interacts with all members of the MAP kinase cascade. *Genetics* **138**, 609–619 (1994).
5. S. Tsunoda *et al.*, A multivalent PDZ-domain protein assembles signalling complexes in a G-protein-coupled cascade. *Nature* **388**, 243–249 (1997).
6. J. D. Scott, T. Pawson, Cell signaling in space and time: Where proteins come together and when they're apart. *Science* **326**, 1220–1224 (2009).
7. T. Pawson, J. D. Scott, Signaling through scaffold, anchoring, and adaptor proteins. *Science* **278**, 2075–2080 (1997).
8. M. C. Good, J. G. Zalatan, W. A. Lim, Scaffold proteins: Hubs for controlling the flow of cellular information. *Science* **332**, 680–686 (2011).
9. R. P. Bhattacharyya, A. Reményi, B. J. Yeh, W. A. Lim, Domains, motifs, and scaffolds: The role of modular interactions in the evolution and wiring of cell signaling circuits. *Annu. Rev. Biochem.* **75**, 655–680 (2006).
10. M. S. Cortese, V. N. Uversky, A. K. Dunker, Intrinsic disorder in scaffold proteins: Getting more from less. *Prog. Biophys. Mol. Biol.* **98**, 85–106 (2008).
11. A. Whitmarsh, The JIP family of MAPK scaffold proteins. *Biochem. Soc. Trans.* **34**, 828–832 (2006).
12. J. Yasuda, A. J. Whitmarsh, J. Cavanagh, M. Sharma, R. J. Davis, The JIP group of mitogen-activated protein kinase scaffold proteins. *Mol. Cell. Biol.* **19**, 7245–7254 (1999).
13. M. Dickens *et al.*, A cytoplasmic inhibitor of the JNK signal transduction pathway. *Science* **277**, 693–696 (1997).
14. A. Whitmarsh, L. Cavanagh, C. Tournier, L. Yasuda, R. Davis, Mammalian scaffold complex that selectively mediates MAP kinase activation. *Science* **281**, 1671–1674 (1998).
15. D. Nihalani, D. Meyer, S. Pajni, L. B. Holzman, Mixed lineage kinase-dependent JNK activation is governed by interactions of scaffold protein JIP with MAPK module components. *EMBO J.* **20**, 3447–3458 (2001).
16. D. Nihalani, H. N. Wong, L. B. Holzman, Recruitment of JNK to JIP1 and JNK-dependent JIP1 phosphorylation regulates JNK module dynamics and activation. *J. Biol. Chem.* **278**, 28694–28702 (2003).
17. C. D'Ambrosio *et al.*, Hyperphosphorylation of JNK-interacting protein 1, a protein associated with Alzheimer disease. *Mol. Cell. Proteomics* **5**, 97–113 (2006).
18. C. Morel *et al.*, Requirement of JIP1-mediated c-Jun N-terminal kinase activation for obesity-induced insulin resistance. *Mol. Cell. Biol.* **30**, 4616–4625 (2010).
19. J. Heo *et al.*, Structural basis for the selective inhibition of JNK1 by the scaffolding protein JIP1 and SP600125. *EMBO J.* **23**, 2185–2195 (2004).
20. J. D. Laughlin *et al.*, Structural mechanisms of allostery and autoinhibition in JNK family kinases. *Structure* **20**, 2174–2184 (2012).
21. T. Tanoue, E. Nishida, Docking interactions in the mitogen-activated protein kinase cascades. *Pharmacol. Ther.* **93**, 193–202 (2002).
22. A. Zeke, M. Misheva, A. Reményi, M. A. Bogoyevitch, JNK signaling: Regulation and functions based on complex protein-protein partnerships. *Microbiol. Mol. Biol. Rev.* **80**, 793–835 (2016).
23. L. Bardwell, Mechanisms of MAPK signalling specificity. *Biochem. Soc. Trans.* **34**, 837–841 (2006).
24. A. J. Bardwell, E. Frankson, L. Bardwell, Selectivity of docking sites in MAPK kinases. *J. Biol. Chem.* **284**, 13165–13173 (2009).
25. Á. Garai *et al.*, Specificity of linear motifs that bind to a common mitogen-activated protein kinase docking groove. *Sci. Signal.* **5**, ra74 (2012).
26. J. Kragelj *et al.*, Structure and dynamics of the MKK7-JNK signaling complex. *Proc. Natl. Acad. Sci. U.S.A.* **112**, 3409–3414 (2015).
27. E. Delaforge *et al.*, Deciphering the dynamic interaction profile of an intrinsically disordered protein by NMR exchange spectroscopy. *J. Am. Chem. Soc.* **140**, 1148–1158 (2018).
28. J. Kragelj *et al.*, Enthalpy–entropy compensation in the promiscuous interaction of an intrinsically disordered protein with homologous protein partners. *Biomolecules* **11**, 1204 (2021).
29. T. Tanoue, M. Adachi, T. Moriguchi, E. Nishida, A conserved docking motif in MAP kinases common to substrates, activators and regulators. *Nat. Cell Biol.* **2**, 110–116 (2000).
30. T. Tanoue, R. Maeda, M. Adachi, E. Nishida, Identification of a docking groove on ERK and p38 MAP kinases that regulates the specificity of docking interactions. *EMBO J.* **20**, 466–479 (2001).
31. A. J. Bardwell, L. Bardwell, Two hydrophobic residues can determine the specificity of mitogen-activated protein kinase docking interactions. *J. Biol. Chem.* **290**, 26661–26674 (2015).
32. T. Lee *et al.*, Docking motif interactions in MAP kinases revealed by hydrogen exchange mass spectrometry. *Mol. Cell* **14**, 43–55 (2004).
33. D. Jacobs, D. Glossip, H. Xing, A. J. Muslin, K. Kornfeld, Multiple docking sites on substrate proteins form a modular system that mediates recognition by ERK MAP kinase. *Genes Dev.* **13**, 163–175 (1999).
34. D. A. Fantz, D. Jacobs, D. Glossip, K. Kornfeld, Docking sites on substrate proteins direct extracellular signal-regulated kinase to phosphorylate specific residues. *J. Biol. Chem.* **276**, 27256–27265 (2001).
35. A. Galanis, S. H. Yang, A. D. Sharrocks, Selective targeting of MAPKs to the ETS domain transcription factor SAP-1. *J. Biol. Chem.* **276**, 965–973 (2001).
36. L. O. Murphy, S. Smith, R.-H. Chen, D. C. Fingar, J. Blenis, Molecular interpretation of ERK signal duration by immediate early gene products. *Nat. Cell Biol.* **4**, 556–564 (2002).
37. K. Kirsch *et al.*, Co-regulation of the transcription controlling ATF2 phosphoswitch by JNK and p38. *Nat. Commun.* **11**, 5769 (2020).
38. R. Hendus-Altenburger *et al.*, The human Na^+/H^+ exchanger 1 is a membrane scaffold protein for extracellular signal-regulated kinase 2. *BMC Biol.* **14**, 31 (2016).
39. A. Mylona *et al.*, Opposing effects of Elk-1 multisite phosphorylation shape its response to ERK activation. *Science* **354**, 233–237 (2016).
40. A. Piserchio *et al.*, Local destabilization, rigid body, and fuzzy docking facilitate the phosphorylation of the transcription factor Ets-1 by the mitogen-activated protein kinase ERK2. *Proc. Natl. Acad. Sci. U.S.A.* **114**, E6287–E6296 (2017).
41. O. Kristensen *et al.*, A unique set of SH3-SH3 interactions controls IB1 homodimerization. *EMBO J.* **25**, 785–797 (2006).
42. L. Mariño Pérez *et al.*, Visualizing protein breathing motions associated with aromatic ring flipping. *Nature* **602**, 695–700 (2022).

43. Z. Dosztányi, V. Csizmok, P. Tompa, I. Simon, IUPred: Web server for the prediction of intrinsically unstructured regions of proteins based on estimated energy content. *Bioinformatics* **21**, 3433–3434 (2005).
44. M. R. Jensen *et al.*, Structural description of the Nipah virus phosphoprotein and its interaction with STAT1. *Biophys J.* **118**, 2470–2488 (2020).
45. S. Naudi-Fabra *et al.*, An extended interaction site determines binding between AP180 and AP2 in clathrin mediated endocytosis. *Nat. Commun.* **15**, 5884 (2024).
46. P. S. Millard *et al.*, IDDomainSpotter: Compositional bias reveals domains in long disordered protein regions—Insights from transcription factors. *Protein Sci.* **29**, 169–183 (2020).
47. J. A. Marsh, V. K. Singh, Z. Jia, J. D. Forman-Kay, Sensitivity of secondary structure propensities to sequence differences between alpha- and gamma-synuclein: Implications for fibrillation. *Protein Sci.* **15**, 2795–2804 (2006).
48. M. Akke, A. G. Palmer, Monitoring macromolecular motions on microsecond to millisecond time scales by $R_{1\rho}$—R_1 constant relaxation time NMR spectroscopy. *J. Am. Chem. Soc.* **118**, 911–912 (1996).
49. D. F. Hansen, P. Vallurupalli, L. E. Kay, An improved ^{15}N relaxation dispersion experiment for the measurement of millisecond time-scale dynamics in proteins. *J. Phys. Chem. B* **112**, 5898–5904 (2008).
50. A. Zeke *et al.*, Systematic discovery of linear binding motifs targeting an ancient protein interaction surface on MAP kinases. *Mol. Syst. Biol.* **11**, 837 (2015).
51. X. Liu *et al.*, A conserved motif in JNK/p38-specific MAPK phosphatases as a determinant for JNK1 recognition and inactivation. *Nat. Commun.* **7**, 10879 (2016).
52. N. R. Skrynnikov, F. W. Dahlquist, L. E. Kay, Reconstructing NMR spectra of "invisible" excited protein states using HSQC and HMQC experiments. *J. Am. Chem. Soc.* **124**, 12352–12360 (2002).
53. S. Lee *et al.*, Examining docking interactions on ERK2 with modular peptide substrates. *Biochemistry* **50**, 9500–9510 (2011).
54. A. Piserchio *et al.*, Structural and dynamic features of F-recruitment site driven substrate phosphorylation by ERK2. *Sci. Rep.* **5**, 11127 (2015).
55. N. S. González-Foutel *et al.*, Conformational buffering underlies functional selection in intrinsically disordered protein regions. *Nat. Struct. Mol. Biol.* **29**, 781–790 (2022).
56. H.-X. Zhou, Polymer models of protein stability, folding, and interactions. *Biochemistry* **43**, 2141–2154 (2004).
57. M. Kjaergaard, J. Glavina, L. B. Chemes, "Predicting the effect of disordered linkers on effective concentrations and avidity with the 'C_{eff} calculator' app" in *Methods in Enzymology*, Linkers in Biomacromolecules, M. Merkx, Ed. (Academic Press, 2021), pp. 145–171.
58. L. Mariño Pérez *et al.*, Structural basis of homodimerization of the JNK scaffold protein JIP2 and its heterodimerization with JIP1. *Structure* **32**, 1394–1403.e5 (2024).
59. V. Modi, R. L. Dunbrack, Defining a new nomenclature for the structures of active and inactive kinases. *Proc. Natl. Acad. Sci. U.S.A.* **116**, 6818–6827 (2019).
60. D. L. Sheridan, Y. Kong, S. A. Parker, K. N. Dalby, B. E. Turk, Substrate discrimination among mitogen-activated protein kinases through distinct docking sequence motifs. *J. Biol. Chem.* **283**, 19511–19520 (2008).
61. P. D. Mace *et al.*, Structure of ERK2 bound to PEA-15 reveals a mechanism for rapid release of activated MAPK. *Nat. Commun.* **4**, 1681 (2013).
62. W. Borcherds *et al.*, Optimal affinity enhancement by a conserved flexible linker controls p53 mimicry in MdmX. *Biophys. J.* **112**, 2038–2042 (2017).
63. H. X. Zhou, The affinity-enhancing roles of flexible linkers in two-domain DNA-binding proteins. *Biochemistry* **40**, 15069–15073 (2001).
64. J. Zhang, B. Zhou, C.-F. Zheng, Z.-Y. Zhang, A bipartite mechanism for ERK2 recognition by its cognate regulators and substrates. *J. Biol. Chem.* **278**, 29901–29912 (2003).
65. A. Piserchio *et al.*, Solution NMR insights into docking interactions involving inactive ERK2. *Biochemistry* **50**, 3660–3672 (2011).
66. M. A. Rainey, K. Callaway, R. Barnes, B. Wilson, K. N. Dalby, Proximity-induced catalysis by the protein kinase ERK2. *J. Am. Chem. Soc.* **127**, 10494–10495 (2005).
67. M. Fu, E. L. F. Holzbaur, JIP1 regulates the directionality of APP axonal transport by coordinating kinesin and dynein motors. *J. Cell. Biol.* **202**, 495–508 (2013).
68. D. S. Im *et al.*, Cdk5-mediated JIP1 phosphorylation regulates axonal outgrowth through Notch1 inhibition. *BMC Biol.* **20**, 115 (2022).
69. T. Orand, E. Delaforge, A. Palencia, M. R. Jensen, Structure of the bipartite JNK1-JIP1 complex. Protein Data Bank. https://www.rcsb.org/structure/9FT9. Deposited 24 June 2024.
70. T. Orand, E. Delaforge, M. Jensen, Backbone 1H, 13C and 15N chemical shift assignments for human JIP1 1–145. BMRB. https://bmrb.io/52858. Deposited 15 January 2025.
71. T. Orand, E. Delaforge, M. Jensen, Backbone 1H, 13C and 15N chemical shift assignments for human JIP1 116–266. BMRB. https://bmrb.io/52859. Deposited 15 January 2025.
72. T. Orand, E. Delaforge, M. Jensen, Backbone 1H, 13C and 15N chemical shift assignments for human JIP1 245–372. BMRB. https://bmrb.io/52860. Deposited 15 January 2025.
73. T. Orand, E. Delaforge, M. Jensen, Backbone 1H, 13C and 15N chemical shift assignments for human JIP1 353–553. BMRB. https://bmrb.io/52861. Deposited 15 January 2025.